Biomedical Engineering Advances 3 (2022) 100031

Contents lists available at ScienceDirect

Biomedical Engineering Advances

journal homepage: www.elsevier.com/locate/bea

Development of magnetic nanoparticles for the intracellular delivery of miR-148b in non-small cell lung cancer

Julien H. Arrizabalaga[a], Jonathan S. Casey[a], Jeffrey C. Becca[b], Yiming Liu[a], Lasse Jensen[b], Daniel J. Hayes[a,c,d,*]

[a] *The Department of Biomedical Engineering, The Pennsylvania State University, University Park, PA 16802, United States*
[b] *The Department of Chemistry, The Pennsylvania State University, University Park, PA 16802, United States*
[c] *Materials Research Institute, Millennium Science Complex, The Pennsylvania State University, University Park, PA 16802, United States*
[d] *The Huck Institute of the Life Sciences, Millennium Science Complex, The Pennsylvania State University, University Park, PA 16802, United States*

ARTICLE INFO

Keywords:
Diels-Alder
Controlled release
Iron oxide
Magnetic nanoparticles
MicroRNAs
Non-small cell lung cancer

ABSTRACT

In this study, we describe the development of an alternating magnetic field radiofrequency (AMF-RF) mediated siRNA delivery platform for the intracellular release of miRNA mimic in A549 cells. Iron oxide nanoparticles were synthesized with discrete chemical attachment sites for the conjugation of payloads. The delivery of the miRNA mimic was controlled by a thermally labile Diels-Alder linker, tethering the oligonucleotide to the surface in an inactive state. The Diels Alder linker acted as an effective control switch to spatiotemporally deliver the therapeutic payload via AMF-RF stimulation. Using confocal microscopy imaging, we demonstrated nanoparticle uptake and controlled intracellular release of the miR-148b mimic from the nanoparticles when stimulated with AMF-RF. Additionally, cell viability and proliferation assays indicated a significant reduction in cancer cells compared to control groups.

1. Introduction

In the United States, lung cancer is responsible for over 100,000 deaths annually, with an economic cost estimated to be over 10 billion dollars a year [1–3]. Lung cancer is the leading cause of cancer death in the United States, responsible for 1 in 4 cancer deaths [3]. As the US population ages and increases in size, the occurrence of lung cancer is expected to increase. While smoking cessation and control of relevant environmental factors are the primary aspects to reduce the incidence of lung cancer, an enormous need still exists for an effective and reliable treatment for this disease [4,5]. Emerging new therapeutics may hold the answer in addressing these issues.

Over the last several decades, interfering RNA molecules known as RNAi have been examined as potential new therapeutics for treating high morbidity and mortality cancers. Short non-coding single stranded RNA (21-22 nucleotides) known as microRNA (miRNA) are involved in the regulation of larger RNA molecules and modulate protein expression in cells. These molecules have been investigated for their anti-cancer properties and use as potential therapeutics [6–11]. In addition, different types of miRNA mimic nano-carriers have been used as delivery vehicles for cancer treatment. Strategies used to spatially and temporally control the delivery of miRNA mimics have been diverse and include visible light, near-IR light, and ultrasound. For instance, miR-34a mimic was encapsulated in poly(lactic-co-glycolic acid) (PLGA) with ammonium bicarbonate, and near-IR light (>780 nm) was used for the controlled release of miR-34a mimic and elimination of human prostate cancer cells [12,13]. In another study using PLGA and ultrasound, controlled delivery of miR-122 mimic, anti-miR-21 mimic, and doxorubicin (DOX) was used to treat liver cancer in mice [14]. Combinatorial therapy of miRNA mimics increased the efficacy of DOX and reduced tumor size [14–17].

Delivery of miR-148b mimic to transgenic mice with HRasG12V-driven skin tumors using silver nanoparticles and light activation as a delivery vehicle was reported [18]. The plasmonic nanoparticles generated heat via the photothermal effect after irradiation, causing the Diels-Alder cycloadduct on the nanoparticle surface to undergo a retro-Diels-Alder reaction releasing the conjugated miR-148b mimic payload. This study provided a framework for the effective controlled delivery and release of the miR-148b mimic to a localized tumor using light activation.

Longer wavelengths of light have been used for the controlled delivery of chemo-therapeutics. AMF-RF triggered delivery of anti-cancer drugs such as doxorubicin (DOX) and erlotinib have also been investigated [19,20]. Additionally, hyperthermia has been performed in cancer

---

[*] Corresponding author at: The Department of Biomedical Engineering, The Pennsylvania State University, University Park, PA 16802, United States.
E-mail address: djh195@psu.edu (D.J. Hayes).

https://doi.org/10.1016/j.bea.2022.100031
Received 6 October 2021; Received in revised form 21 March 2022; Accepted 24 March 2022

tissues via magnetic nanoparticle heating, as well as combinatorial therapy [21,22]. Although these therapies have shown promise, they often suffer from a multitude of drawbacks and limitations.

Use of the appropriate alternating magnetic field radiofrequency (AMF-RF) triggered technology coupled with RNAi based therapeutics addresses many of the drawbacks of previous oligonucleotide delivery systems. The combination of AMF-RF and magnetic nanoparticles leads to a localized heating of the nanoparticles. This enables the activation of therapeutics with increased tissue penetration, reduced trapping of heat in tissues, and use of biocompatible magnetic nanoparticles. Retro Diels-Alder reactions have a well-defined energy barrier which permits a predictable controlled release [23]. This results in a more direct relationship between the energy delivered (in the form of hysteretic heating) and the amount of therapeutic released. Additionally, use of miRNA mimics compared to traditional chemotherapeutics has the advantages of targeting multiple conserved pathways, and decreasing off-target effects when coupled with a delivery vehicle that enables tissue-specific targeting [24].

In this study, the controlled release of miR-148b mimic using AMF-RF triggered release in A549 non-small cell lung cancer cells was investigated. This research sought to build on previous work in controlled delivery of miRNA mimics [18]. miR-148b mimic was tethered to the surface of magnetic iron oxide nanoparticles using a Diels-Alder cycloadduct. A549 cells were transfected with the magnetic nanoparticle-miRNA mimic conjugates. The modified nanoparticles were then excited using an externally applied alternating magnetic field radiofrequency to drive the hysteretic heating and induce the controlled release of the miR-148b mimic intracellularly.

2. Materials and methods

2.1. Materials and reagents

Iron (II) chloride tetrahydrate (98%), iron (III) chloride hexahydrate (≥98%), hydrochloric acid (HCl, ACS Reagent, 37%), ethanol (≥99.5%), nitric acid (ACS Reagent, 70%), ammonium hydroxide solution (NH_4OH, ACS reagent, 28.0-30.0% NH_3 basis), dichloromethane (>99.8%), methanol (anhydrous, 99.8%), 2-furanmethanethiol (98%), 6-maleimidohexanoic acid (90%), (3-aminopropyl)triethoxysilane (APTES, 99%), N-hydroxysuccinimide (NHS, 98%), methanol-d4 (≥99.8 atom % D), Cell Counting Kit-8 (CCK-8), A549 cells (Human Caucasian Lung Carcinoma), and Proteinase K (from Tritirachium album, ≥ 30 units/mg protein) were purchased from Millipore Sigma (St Louis, MO). Sodium hydroxide (≥98%) was acquired from Honeywell Fluka (Morris Plains, NJ). Sulfo-SMCC (Sulfosuccinimidyl-4 (N-maleimidomethyl) Cyclohexane-1-carboxylate) was obtained from Pierce Biotechnology (Rockford, IL). Dulbecco's Phosphate Buffered Saline (PBS) was bought from Cytiva (Pittsburgh, PA). Fetal bovine serum (FBS) was acquired from Corning (Corning, NY). Cell culture dishes (35 mm diameter, glass bottom, 1 or 4 compartments) were obtained from Greiner Bio-One (Monroe, NC). LIVE/DEAD Viability/Cytotoxicity kit, Quant-iT PicoGreen dsDNA assay kit, CellTracker Red CMTPX Dye, 1-ethyl-3-(3-dimethylaminopropyl)carbodiimide hydrochloride (EDC), Dulbecco's Modified Eagle Medium (DMEM), Opti-MEM Reduced-Serum Medium, antibiotic-antimycotic, DEPC-treated water, and isopropanol (≥99.5%), were purchased from Thermo Fisher Scientific (Waltham, MA). Custom amine-modified oligonucleotides (miR-148b: 5' 6-FAM 2'OMe UCA GUG CAU CAC AGA ACU UUG U C6-NH2 3') tagged with FAM (Fluorescein) were acquired from Integrated DNA Technologies (Coralville, IA). All reagents were used as received.

2.2. Computational methods

All density functional theory (DFT) calculations were performed using the NWChem 6.8 software package [25]. All geometry optimizations and frequency calculations were performed using the B3LYP functional and a 6-311g* basis set [26–29]. The numerical grid settings were set to extra fine and all optimizations were performed using tight convergence criteria for the gradient, gradient maximum, root mean square, and Cartesian step maximum. A reduced atom model was used for the maleimide to reduce computational effort and ensure no negative vibrational modes were found for the products and reactants, and just a single negative vibrational mode for transition states. Transition state searches were performed by using optimized structures of the reactants initially constrained to 2.4 Å apart measured at bond forming carbon atoms. The thermodynamic data was obtained during the normal mode analysis simulations at 25, 40, 60, and 80 °C. All simulations were performed excluding any solvent effects.

2.3. Synthesis of Diels-Alder linker

The cycloaddition reaction between 2-furanmethanethiol and 6-maleimidohexanoic acid is illustrated in **Fig. 1**. This Diels-Alder cycloadduct was synthesized as previously reported [23,30]. Briefly, 6-Maleimidohexanoic acid (1.6 g) was dissolved in methanol (10 mL) and dichloromethane (10 mL) in a glass vial. 2-Furanmethanethiol (380 µL) was then added to the mixture. The vial was sealed, protected from light using aluminum foil, and the reaction allowed to proceed for 7 days at room temperature under agitation.

2.4. Synthesis of iron oxide nanoparticles

Iron oxide nanoparticles were synthesized by coprecipitation of Fe^{2+} and Fe^{3+} ions in presence of NH_4OH as previously reported [31–34]. Briefly, 2 mL of $FeCl_2 \cdot 4\,H_2O$ (0.93 g) dissolved in 1M HCl and 4 mL of $FeCl_3 \cdot 6H_2O$ (2.16 g) dissolved in 1M HCl were combined with 54 mL of deionized water in a round-bottom flask heated at 95 °C. NH_4OH (12.5 mL of 28% NH_3 in H_2O solution) was slowly added and the mixture vigorously stirred for an hour. The solution was cooled down, and 1M nitric acid was added to adjust the pH between 4 and 7. The mixture was then allowed to incubate at room temperature for 24 h. The nanoparticles were separated from the supernatant by centrifugation (30 min, 1300 xg), and thoroughly washed three times with deionized water before getting dried. The X-ray diffraction patterns of the Fe_3O_4 nanoparticles were obtained using a Malvern Panalytical Empyrean (3rd gen.) equipped with a Co source. Fe_3O_4 nanoparticles were also characterized using both an FEI Tecnai G20 20 XTWIN, and a Talos F200X transmission electron microscope with EDX mapping. The magnetization of the nanoparticles was measured at 305 K using a Quantum Design MPMS system.

2.5. Functionalization of nanoparticles

The general functionalization protocol from unmodified iron oxide nanoparticles to nanoparticles functionalized with miR-148b mimic is shown in **Fig. 2**.

2.5.1. Silanization

The iron oxide nanoparticles were first functionalized by silanization following a previously established procedure [35]. Briefly, 10 mg of iron oxide nanoparticles were dispersed by sonication in ethanol (20 mL) and water (133 μL). APTES (5.4 μL) was added to the mixture and the pH adjusted between 6 and 7 using 1M HCl. The sealed polypropene tube containing the solution was then placed on a rocker and mechanically agitated for 7 h at room temperature. The nanoparticles were separated from the supernatant after centrifugation (10 min, 1200 xg), redispersed by sonication in anhydrous ethanol, and these washing steps repeated three times. After the final wash, the nanoparticles were dried under vacuum at room temperature for 8 to 12 h.

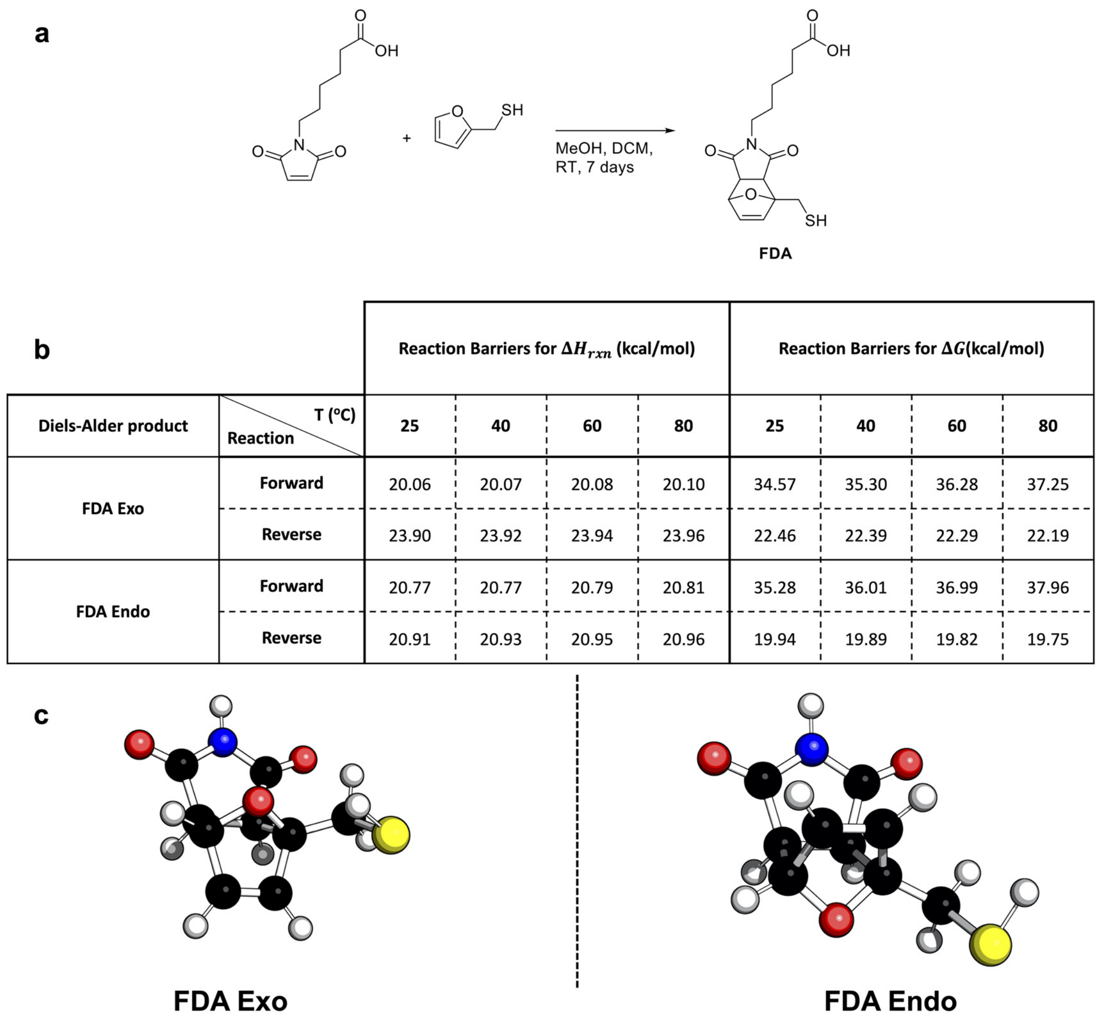

Diels-Alder product	Reaction \ T (°C)	Reaction Barriers for ΔH_{rxn} (kcal/mol) 25	40	60	80	Reaction Barriers for ΔG(kcal/mol) 25	40	60	80
FDA Exo	Forward	20.06	20.07	20.08	20.10	34.57	35.30	36.28	37.25
	Reverse	23.90	23.92	23.94	23.96	22.46	22.39	22.29	22.19
FDA Endo	Forward	20.77	20.77	20.79	20.81	35.28	36.01	36.99	37.96
	Reverse	20.91	20.93	20.95	20.96	19.94	19.89	19.82	19.75

Fig. 1. (a) Cycloaddition reaction between 2-furanmethanethiol and 6-maleimidohexanoic acid. (b) Gibbs free energy and enthalpy reaction barriers generated from B3LYP/6-311G* theory. (c) Structures of endo and exo products for FDA used for B3LYP/6-311G* computation. Black atoms: Carbon; White: Hydrogen; Yellow: Sulfur; Blue: Nitrogen; Red: Oxygen. Images rendered using the software PyMOL. Transition states are reported in the Supplementary Material Fig. S1. (For interpretation of the references to color in this figure legend, the reader is referred to the web version of this article).

2.5.2. *Conjugation of sulfo-SMCC*

Iron oxide nanoparticles modified with APTES were dispersed by sonication in ethanol (5 mL) and PBS (5 mL). The pH of the solution was adjusted between 7.2 and 7.5 before adding Sulfo-SMCC (37 mg), sealing the polypropene tube containing the solution, and mechanically agitating it for 8 h on a rocker at room temperature. The nanoparticles were then centrifuged (10 min, 1200 xg), and washed with deionized water three times.

2.5.3. *Conjugation of Diels-Alder linker*

Iron oxide nanoparticles previously modified with Sulfo-SMCC were redispersed by sonication in a 70/30 (v/v) ethanol/water mixture (9 mL). The Diels-Alder solution (2 mL) prepared in advance was then added to the mixture. The pH of the solution was adjusted between 6.5 and 7.5 using 1M NaOH. The mixture was protected from light using aluminum foil and mechanically agitated for 12 h. The nanoparticles were then centrifuged (10 min, 1200 xg) and washed three times with isopropanol.

2.5.4. *Conjugation of miRNA mimic*

miR-148b mimic was conjugated as previously described [18,30]. Iron oxide nanoparticles (5 mg) were resuspended by sonication in isopropanol (4.5 mL) before adding EDC/NHS (500 µL of a stock 100 mM solution in DI water). The mixture was mechanically agitated for 15 min before adding the 3' amine miRNA mimic (50 µL of a stock 100 µM solution in RNase-free water). The solution was placed on a rocker for 8 to 12 h to allow for covalent coupling. The nanoparticles were then centrifuged (10 min, 1200 xg), washed once with RNase-free water, and three times with sterile PBS prior to use. Zeta potential measurements of the nanoparticles were carried out in PBS with a Malvern Zetasizer Nano ZS to monitor the change in surface charge at each conjugation step.

2.6. *Immersion heating*

Iron oxide nanoparticles functionalized with miR-148b mimic FAM were redispersed in PBS at a concentration of 50 ppm. Sealed microcentrifuge tubes with 1 mL of nanoparticles in PBS were prepared and heated in an oil bath at 80 °C for 4 h to trigger the retro Diels-Alder reaction and release the miR-148b mimic [23]. After immersion heating, samples were centrifuged (10 min, 1200 xg), and three 200 µL aliquots of the supernatant were pipetted per sample into a 96-well plate. To evaluate the amount of miR-148b mimic released by the retro Diels-Alder reaction (**Fig. 2**), the fluorescence intensity of the FAM conjugated to the miR-148b mimic was measured in each well at 495/520 nm (Excitation/Emission) using a Molecular Devices Spectramax M5 Microplate/Cuvette Reader.

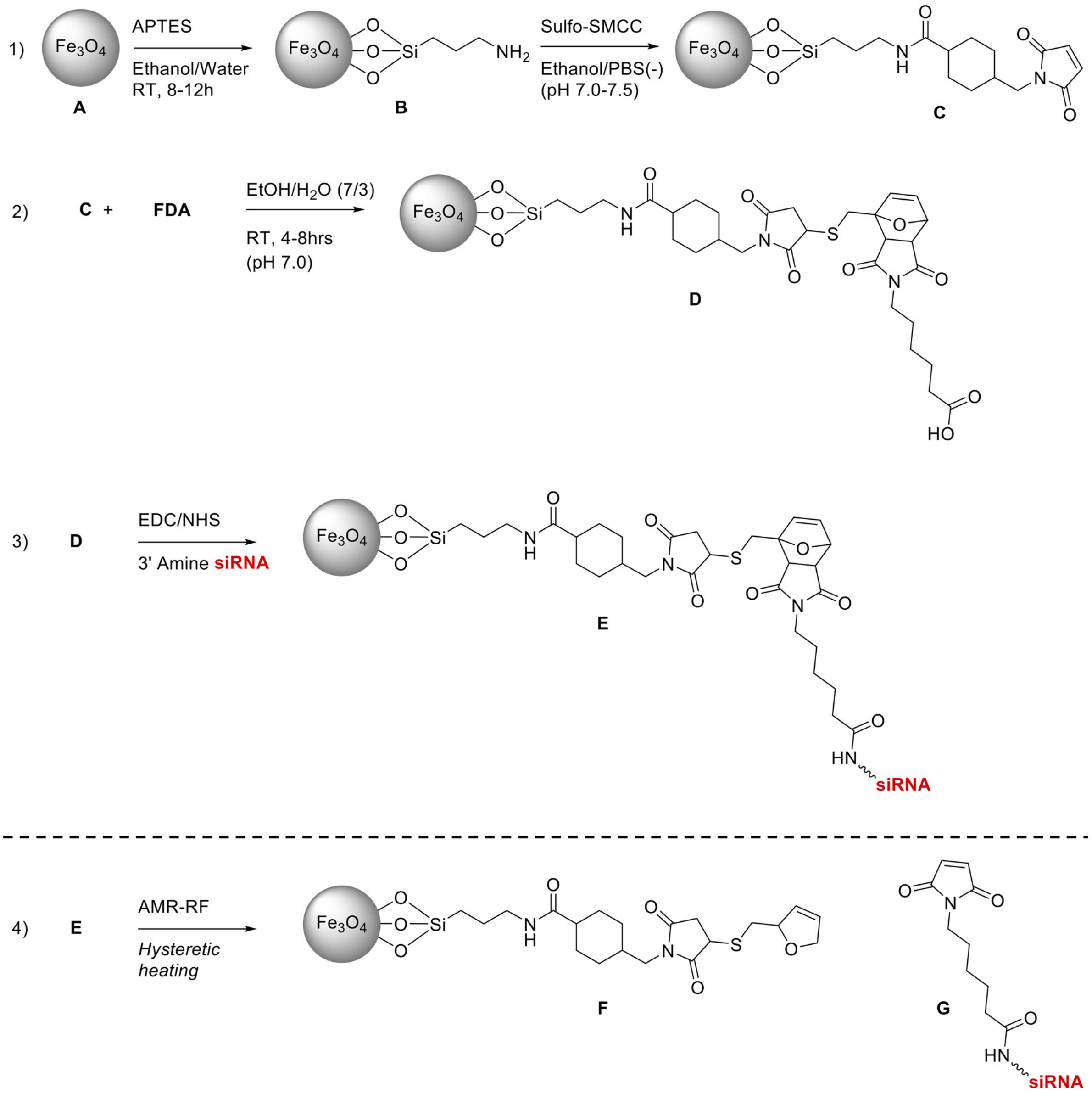

Fig. 2. (1–3): multistep functionalization of Fe_3O_4 nanoparticles. Successive silanization step with APTES, conjugation of Sulfo-SMCC, conjugation of Diels-Alder linker FDA, and conjugation of a 3' Amine siRNA. (4): retro Diels-Alder cleavage reaction triggered by the AMF-RF hysteretic heating and release of the maleimide with conjugated siRNA.

2.7. AMF-RF hysteretic heating

Iron oxide nanoparticles functionalized with miR-148b mimic were redispersed in PBS. The concentration of the nanoparticles was 50 ppm, and the concentration of the miR-148b mimic with FAM was 20 nM. Sealed microcentrifuge tubes with 1 mL of nanoparticles in PBS were prepared and underwent AMF-RF hysteretic heating using a nanoTherics magneTherm [31,34]. The radiofrequency was 628 kHz, the DC power supply current was 7.5 A, and the DC power supply voltage was 31 V. The AMF-RF coil used had a 50 mm diameter and 17 turns. The Alternating Magnetic Field Strength and the Specific Loss Power were determined as previously described [31,34,36,37]. and detailed protocols with equations are reported in the **Supplementary Material**. The system was quasi-adiabatic, the heating device was connected to a recirculating water cooler which maintained the coil temperature at 15 °C during the operation of the equipment. The sample was encased in a Styrofoam receptacle before being inserted in the center of the coil. The sample was consequently evenly heated while also being isolated from any external heat transfer. 4 min, 8 min, 12 min, 16 min, 20 min, and 24 min were compared as durations for the AMF-RF exposure of the samples. Immediately after hysteretic heating, samples were centrifuged (10 min, 1200 xg), and three 200 μL aliquots of the supernatant were pipetted per sample into a 96-well plate. To evaluate the amount of miR-148b mimic released by the retro Diels-Alder reaction (Fig. 2), the fluorescence intensity of the FAM conjugated to the miR-148b mimic was measured in each well at 495/520 nm (Excitation/Emission) using a Molecular Devices Spectramax M5 Microplate/Cuvette Reader.

2.8. Cell culture

A549 cells (Human Caucasian Lung Carcinoma) were cultured in DMEM supplemented with 10% fetal bovine serum and 1% antibiotic-antimycotic. Cell culture flasks were kept in a humidified incubator at 37 °C with 5% CO_2. All experiments were performed with cells at passage 3 or 4.

2.9. Cell viability and proliferation assays

Cell viability was assessed using either a LIVE/DEAD Viability/Cytotoxicity assay or a Cell Counting Kit-8 (CCK-8, WST-8 based) according to the manufacturer's protocols. For the LIVE/DEAD assay, cells were washed with PBS and incubated at 37 °C for 30 min with a 2 μM calcein AM and 4 μM EthD-1 working solution. Cells were then imaged with an Olympus IX73 fluorescence microscope (Olympus, Center Valley, PA). ImageJ (NIH, Bethesda, MD) was used for image processing. Total DNA content was used to determine the cell count as previously described [38]. Proteinase K at a concentration of 0.5 mg/mL was added to the wells and plates were incubated overnight at 56 °C to lyse the cells and release their DNA content. A PicoGreen dsDNA assay kit was used according to the manufacturer's recommendations to quantify the amount of dsDNA per sample. Equal volumes of PicoGreen dsDNA reagent were combined with the volumes of the wells and the fluorescence intensity was then measured in each well at 480/520 nm (Excitation/Emission) using a Molecular Devices Spectramax M5 Microplate/Cuvette Reader.

2.10. AMF-RF mediated release of miR-148b mimic in A549 cells

A549 cells were seeded in 35 mm glass-bottom cell culture dishes (4 compartments) at a density of 0.02×10^6 cells per compartment. After 24 h, the complete DMEM medium was removed and the cells were transfected with the modified nanoparticles (400 µL, 200 ppm, 50 nM miR-148b mimic concentration) or unmodified nanoparticles (400 µL, 200 ppm) in Opti-MEM medium. Cells were allowed to incubate for an hour prior to AMF-RF exposure (23 min exposure time, radiofrequency of 628 kHz, and 21.6 kA/m magnetic field strength). The cell culture medium in the dishes was then replaced with some fresh Opti-MEM. Cell viability and proliferation assays were performed 24 h after exposing the cells to AMF-RF.

2.11. Confocal microscopy for intracellular uptake and release

A549 cells were stained with CellTracker Red CMTPX Dye and seeded in 35 mm glass-bottom cell culture dishes at a density of 0.4×10^6 cells per well. After 24 h, the complete DMEM medium was removed and the cells were transfected with the modified nanoparticles (400 µL, 200 ppm, 50 nM miR-148b mimic concentration) in Opti-MEM medium. Cells were allowed to incubate for an hour prior to AMF-RF exposure for 23 min using the same RF parameters as described in the previous section. The cell culture media in the dishes was then replaced with some fresh Opti-MEM, and the cells were imaged using a Zeiss LSM 880 confocal microscope with FLIM (Zeiss, Oberkochen, Germany). 2 groups were compared to evaluate the intracellular release of the fluorescently labeled miR-148b mimic: cells unstimulated and cells stimulated with AMF-RF. The Mander's coefficient was calculated using the software FIJI as previously described [30]. The background subtraction was performed by selecting a region of interest and subtracting it from the image. The threshold was calculated before running the Coloc 2 plugin. The threshold accounted coefficient for the green channel in which the miR-148b mimic fluorescent label was imaged was specifically used for reporting.

2.12. Statistical analysis

Quantitative results were expressed as mean values ± standard deviation (SD). Sample size (n) is indicated in the figure legends. Statistical analysis was performed via two-way analysis of variance (ANOVA), followed by Tukey's *post hoc* testing. Statistical significance was set at $p < 0.05$. The software GraphPad Prism 8 was used for all statistical analyses.

3. Results and discussion

3.1. Characterization of nanoparticles

The reaction yield for the multistep functionalization of iron oxide nanoparticles shown in **Fig. 2** was 19.2 %. The conjugation efficiency of the miR-148b mimic was 8.4 % and the miRNA mimic loading was 2.5×10^{-10} moles per mg of iron oxide nanoparticles (calculations detailed in the **Supplementary Material**). Transmission electron microscopy (TEM) imaging and X-ray diffraction (XRD) analysis were performed on the synthesized iron oxide nanoparticles to determine their size and composition (**Fig. 3**). The TEM images revealed that the nanoparticles had a nearly spherical shape with sizes ranging from 5 to 15 nm diameter. The Miller indices from the XRD analysis indicated that the nanoparticle sample was composed of magnetite (Fe_3O_4) with a phase purity over 95%. A Rietveld refinement was performed using the analysis software Jade, and the size of the nanoparticles was estimated to be 10.1 ± 0.5 nm in diameter. This value is in agreement with previous studies that reported on iron oxide nanoparticles synthesized by coprecipitation of $Fe_2{}^+$ and $Fe_3{}^+$ ions following the protocol established by Massart et al [32,33,39].

The magnetic hysteresis curves of the synthesized Fe_3O_4 nanoparticles are shown in **Fig. 3**. The magnetic saturation (Ms) observed for these nanoparticles was 77 emu/g. A correlation exists between particle size and magnetic properties of iron oxide nanoparticles [40]. This can have a direct effect on the hysteretic heating of the magnetic nanoparticles since the hysteretic losses are dependent on the magnetic saturation and the anisotropy barrier. Previous studies with iron oxide nanoparticles in size ranging from 9.1 to 13.1 nm in diameter reported Ms between 70 to 90 emu/g, in agreement with the value we observed [41].

Density functional theory (DFT) calculations were used to determine the forward and reverse energy barriers for the furan-based cycloadduct (named FDA) used in this study [42,43]. The enthalpy and Gibbs free energy barriers predicted at different temperatures are reported in **Fig. 1** along with the PyMOL [44] rendered images obtained from the B3LYP/6-311G* computations [26–29]. FDA was purified by reversed-phase high performance liquid chromatography (RP-HPLC) and characterized by NMR spectroscopy and electrospray ionization mass spectrometry (ESI-MS) as reported in the **Supplementary Material**.

Additionally, zeta potential measurements were performed to monitor the multistep functionalization process of the Fe_3O_4 nanoparticles (**Fig. 3**). The changes in surface charge demonstrated the successive conjugation of the Diels-Alder linker and miR-148b mimic. The zeta potential was increasingly negative as a result of the sequential addition of these molecules to the iron oxide nanoparticles. The largest change in zeta potential was seen with the addition of the final nucleic acid addition as a result of the negative charge on the backbone, in agreement with previous nucleic acid functionalization studies [30,45].

3.2. Specific loss power (SLP) as a function of radiofrequency

Specific loss power (SLP) generated by the magnetic iron oxide nanoparticles were determined from calorimetric heating measurements (calculations detailed in the **Supplementary Material**) [37]. A range of different alternating magnetic field radiofrequencies (AMF-RF) were compared to see which one achieved the maximum hysteretic heating of the iron oxide nanoparticles (**Fig. 4**). A radiofrequency increase resulted in a SLP increase with a maximum reached at 628 kHz, with a corresponding alternating magnetic field strength of 21.6 kA/m (calculations detailed in the **Supplementary Material**). In clinical applications involving hyperthermia, a radiofrequency under 300 kHz and intensities under 16 kA/m are recommended to avoid eddy currents and non-specific heating of tissues [46]. As this is a proof-of-concept study evaluating the controlled release of miR-148b mimic *in vitro*, the 628 kHz radiofrequency and magnetic field strength of 21.6 kA/m were

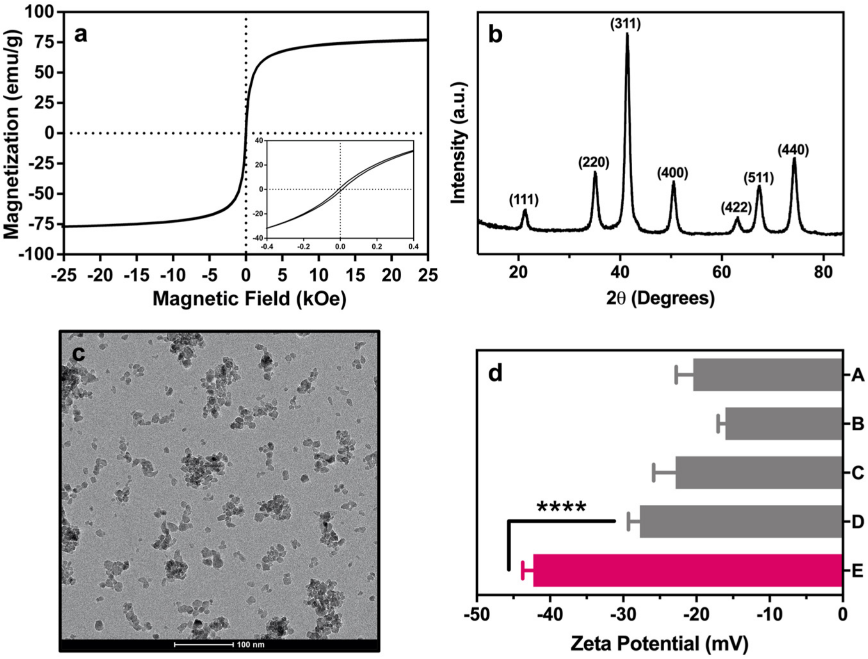

Fig. 3. Characterization of iron oxide nanoparticles. (a) Magnetic hysteresis curves with a zoom in the area of small magnetic fields in the inset panel. (b) X-ray diffraction patterns with representative index on typical peaks. (c) Transmission electron microscopy image of unmodified iron oxide nanoparticles. Additional images and EDS mapping are available in the Supplementary Material Fig. S2. (d) Zeta potential of nanoparticles during the different steps of the modification process ($n = 4$ per group). A, B, C, D, and E refer to the nanoparticle functionalization steps as labeled in Fig. 2. E represents the nanoparticle after conjugation of miR-148b mimic. ****Significant difference ($p < 0.0001$).

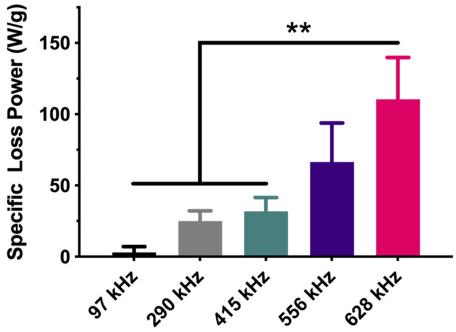

Fig. 4. Specific Loss Power (SLP) as a function of the AMF radiofrequency ($n = 3$ per group). **Significant difference ($p < 0.01$) when compared to 628 kHz.

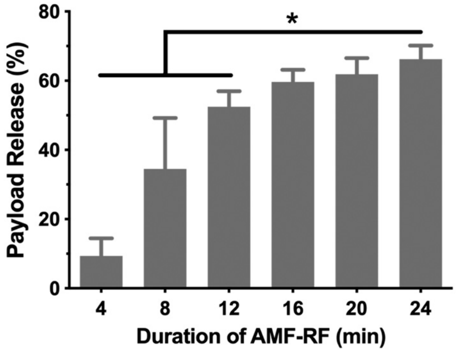

Fig. 5. miR-148b mimic release from iron oxide nanoparticles after AMF-RF hysteretic heating at 21.6 kA/m and 628 kHz ($n = 3$ per group). *Significant difference ($p < 0.05$) when compared to 24 min.

maintained for the rest of the experiments. With these parameters, the SLP measured for the iron oxide nanoparticles was 110 ± 29 W/g. This SLP value was in agreement with those previously reported for iron oxide nanoparticles of similar size under comparable AMF parameters [22,31,32,34,39].

3.3. AMF-RF mediated release of miR-148b mimic from nanoparticles

After determining the optimum AMF radiofrequency, nanoparticles conjugated with FAM labeled miR-148b mimic were exposed to AMF-RF for different times to evaluate the release profile of the miR-148b mimic (**Fig. 5**). The release study was performed with sealed microcentrifuge tubes encased in a custom-made Styrofoam insert to maintain a quasi-adiabatic isolation. The total release was defined as the amount of miR-148b mimic FAM released after immersing the nanoparticles in an oil bath at 80 °C for 6 h (**Supplementary Material Fig. S3**). Previous release studies using a similar furan Diels-Alder linker conjugated to silver nanoparticles showed a complete release after 2 h at 80 °C [23]. Iron oxide nanoparticles were exposed to AMF-RF for up to 24 min. The payload release began to plateau after 16 min (59.7 ± 3.5 %), and no statistical difference could be observed in the release at 20 min (61.9 ± 4.6 %) or 24 min (66.3 ± 3.9 %). This phenomenon has been previously observed in studies where Diels-Alder linkers have been used for controlled payload release [23,31,34]. This plateau in release could be due to differences in the reverse reaction energy barriers of the Diels-Alder endo and exo isomers resulting in preferential cleavage of one isomer at the achieved temperature as reported in **Fig. 1**.

3.4. Intracellular uptake and payload release

Intracellular release experiments were conducted to confirm nanoparticle uptake in A549 cells and controlled miR-148b mimic release inside the cells. A549 cells were stained with Cell Tracker Red CMTPX Dye to provide a cytosolic contrast to the FAM labelled miRNA mimic, enabling quantification via Mander's overlap coefficient. These two specific fluorophores were used to limit overlap between the signals when cells were imaged using confocal microscopy. **Fig. 6** illustrates the colocalization (overlap) existing between the red (Cell Tracker Red dye) and green (FAM on miR-148b mimic) fluorescence of the non AMF-RF activated group versus the AMF-RF activated group. The non AMF-RF activated group showed relatively weak fluorescence from the FAM and poor colocalization between the Cell Tracker Red and the fluorescence emitted from the fluorophore (Mander's Coefficient = 0.42). This is due to the fluorophore being attached to the nanoparticle and not diffused throughout the cell. After AMF-RF activation, the green fluores-

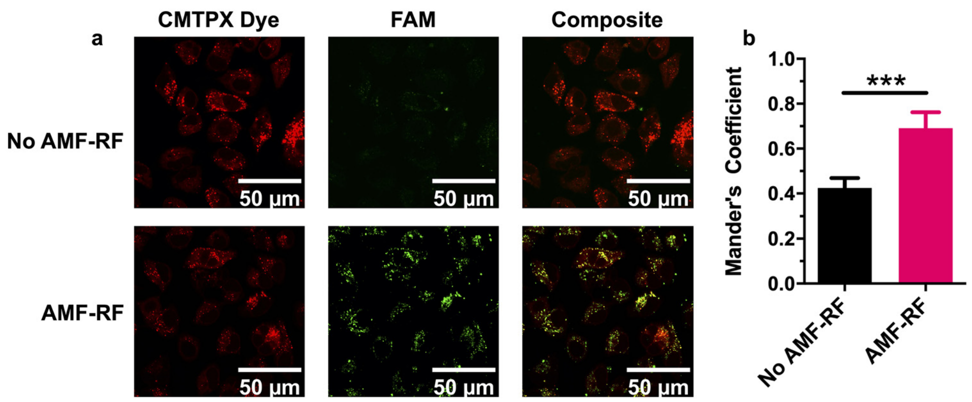

Fig. 6. (a) Confocal microscopy images of A549 cells comparing non AMF-RF activated cells and AMF-RF activated cells. The Red CMTPX cytosolic dye is visible in the Red Channel while the FAM conjugated to the miR-148b mimic is visible in the Green Channel. (b) Images were analyzed using the Mander's coefficient to determine overlap between the green and red channels for both non AMF-RF and AMF-RF groups (*n* = 7 per group). ***Significant difference ($p < 0.001$) (For interpretation of the references to color in this figure legend, the reader is referred to the web version of this article).

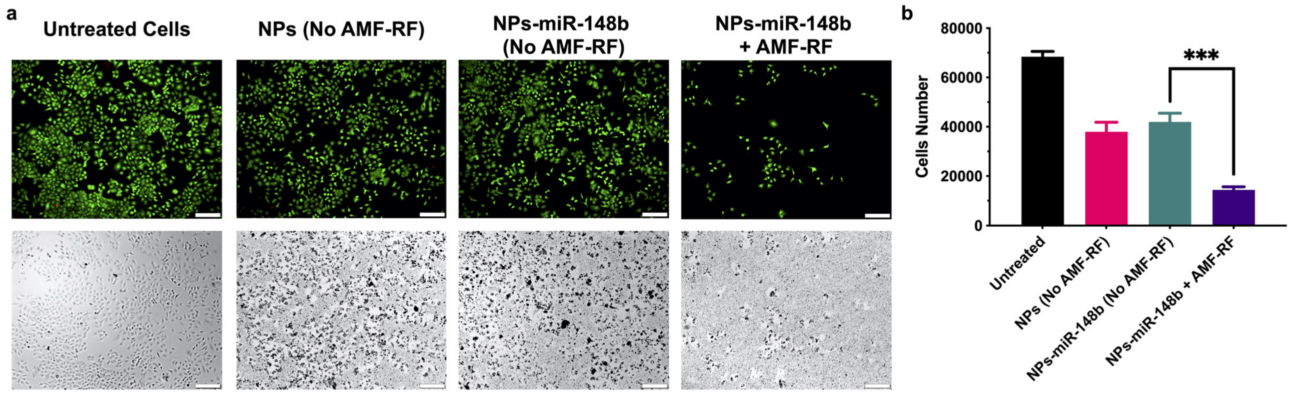

Fig. 7. (a) Representative LIVE/DEAD staining of A549 cells 24 h after AMF-RF exposure. Scale bar = 200 µm. (b) Total cell number (PicoGreen dsDNA assay) 24 h after AMF-RF exposure (*n* = 3 per group). ***Significant difference ($p < 0.001$).

cent signal increased drastically, and colocalization or overlap between the FAM and Cell Tracker Red increased significantly (Mander's Coefficient = 0.69). The increase in fluorescent intensity is likely a result of a reduction in metal induced quenching as the nucleic acid and associated fluorophore diffuse away from the particle after release [47]. This can be seen qualitatively in Fig. 6. In the non AMF-RF activated groups, the green channel showed sparse punctate FAM fluorescence (false colored Green). These experiments indicated a controlled intracellular release of the miR-148b mimic from the iron oxide nanoparticles in response to AMF-RF stimulation.

3.5. AMF-RF mediated release of miR-148b mimic in A549 cells

Cell viability and proliferation assays were performed 24 h after AMF-RF exposure (Fig. 7). The results of the LIVE/DEAD staining and of the PicoGreen dsDNA assays were in agreement with each other. The reduction in viable cells is visualized qualitatively with the Live/Dead staining (Fig. 7**a**). A quantitative assessment showed that A549 cells transfected with iron oxide nanoparticles conjugated with miR-148b mimic and exposed to AMF-RF resulted in a significantly lower number of viable cells (14353 ± 1291) compared to the untreated group (68411 ± 2169), group with unmodified nanoparticles (37898 ± 3877), or group with nanoparticles conjugated with miR-148b mimic but not exposed to AMF-RF (41936 ± 3576) (Fig. 7**b**). Additionally, less nanoparticles could be observed in the experimental group exposed to AMF-RF. It is most likely the result of an increase in cell death resulting in internalized iron oxide nanoparticles being removed from dishes along with dead cells prior to imaging. Cell viability was also assessed using a CCK-8 (WST-8 based) assay (**Supplementary Material Fig. S4**), and the results obtained were in agreement with the LIVE/DEAD staining and the PicoGreen dsDNA assays (Fig. 7). Cell viability as a function of nanoparticle concentration or AMF-RF activation was also investigated (**Supplementary Material Figs. S5 and S6**).

The mechanism and site of delivery of the miRNA mimic is as important as the miRNA mimic chosen to treat the intended cancer. In non-small cell lung cancer cells, the expression of miR-148b was observed to downregulate the expression of a variety of essential cellular proteins. One class of proteins in which miR-148b has demonstrated to affect in non-small cell lung cancer (NSCLC) cells are cell adhesion molecules (CAMs) [48–52]. Cell adhesion molecules are responsible for cell-cell attachment, attachment of cells to surfaces, and migration of cells to other areas of the body. Heightened amounts miR-148b in NSCLC cells (specifically A549) contribute to a decrease in ALCAM and E-Cadherin levels, while increasing N-Cadherin levels. Subsequently, the amount of miR-148b inside these cells were found to be inversely proportional to the survivability of these cell types.

Temporal controlled release of miR-148b mimic in A549 cells has been demonstrated in this study. The chosen AMF-RF conditions and duration of exposure resulted in localized heating of the nanoparticles, cleavage of the Diels-Alder cycloadduct and release of the miR-148b mimic intracellularly in A549 cells. The relatively high concentration of nanoparticles (200 ppm) used for this study was a compromise to increase the concentration of the miR-148b mimic (50 nM) at the expense of the inherent toxicity of the nanoparticles. Future work will take into consideration this limitation and focus on optimizing the loading efficiency of the miRNA mimic onto the nanoparticles. Increasing the size of the iron oxide nanoparticles would also increase the specific loss power, allowing use of a lower radiofrequency and more biocompatible AMF-RF parameters for *in vivo* studies.

4. Conclusions

In this study, we demonstrated a predictable and controlled release of miR-148b mimic from the surface of iron oxide nanoparticles when exposed to an externally applied alternating magnetic field radiofrequency (AMF-RF). Using confocal microcopy, controlled intracellular release of miR-148b mimic was demonstrated by comparing an AMF-RF exposed experimental group versus a non AMF-RF control. Additionally, the AMF-RF exposed group resulted in significantly less cell viability than the non AMF-RF control. This observation indicated that miR-148b mimic was affecting A549 cell viability. Overall, this magnetic siRNA nanocarrier demonstrated an effective and efficient way of attaching miRNA mimic payloads to the surface of iron oxide nanoparticles, with predictable release inside cells when exposed to an externally applied alternating magnetic field.

Declaration of Competing Interest

The authors declare that they have no known competing financial interests or personal relationships that could have appeared to influence the work reported in this paper.

Acknowledgments

This work was supported by the Office of the Assistant Secretary of Defense for Health Affairs through the Peer Reviewed Medical Research Program under Award No. W81XWH-18-1-0115. Opinions, interpretations, conclusions and recommendations are those of the author and are not necessarily endorsed by the Department of Defense. Dr. Hayes and Dr. Casey acknowledge support from the National Institute of Dental and Craniofacial Research of the National Institutes of Health under award number RDE024790A. LJ and JCB gratefully acknowledge financial support from National Science Foundation Grant CHE-1856419 and NRT-1449785. Simulations in this work were conducted in part with Advanced Cyber infrastructure computational resources provided by the Institute for Computational and Data Sciences at The Pennsylvania State University (University Park, PA).

Supplementary materials

Supplementary material associated with this article can be found, in the online version, at doi:10.1016/j.bea.2022.100031.

References

[1] S.J. Seung, M. Hurry, S. Hassan, R.N. Walton, W.K. Evans, Cost-of-illness study for non-small-cell lung cancer using real-world data, Curr. Oncol. 26 (2) (2019) 102–107.
[2] A.B. Mariotto, K. Robin Yabroff, Y. Shao, E.J. Feuer, M.L. Brown, Projections of the cost of cancer care in the United States: 2010–2020, JNCI J. Natl. Cancer Inst. 103 (2) (2011) 117–128.
[3] R.L. Siegel, K.D. Miller, H.E. Fuchs, A. Jemal, Cancer statistics, 2021, CA Cancer J. Clin. 71 (1) (2021) 7–33.
[4] K.C. Arbour, G.J. Riely, Systemic therapy for locally advanced and metastatic non–small cell lung cancer, JAMA 322 (8) (2019) 764.
[5] J.A. Barta, C.A. Powell, J.P. Wisnivesky, Global epidemiology of lung cancer, Ann. Glob. Health 85 (1) (2019).
[6] N.S. Gandhi, R.K. Tekade, M.B. Chougule, Nanocarrier mediated delivery of siRNA/miRNA in combination with chemotherapeutic agents for cancer therapy: current progress and advances, J. Control. Release 194 (2014) 238–256.
[7] Y. Peng, C.M. Croce, The role of MicroRNAs in human cancer, Signal Transduct. Target. Ther. 1 (1) (2016) 15004.
[8] G.A. Calin, C.M. Croce, MicroRNAs and chromosomal abnormalities in cancer cells, Oncogene 25 (46) (2006) 6202–6210.
[9] Y. Xu, F. Xia, L. Ma, J. Shan, J. Shen, Z. Yang, J. Liu, Y. Cui, X. Bian, P. Bie, C. Qian, MicroRNA-122 sensitizes HCC cancer cells to adriamycin and vincristine through modulating expression of MDR and inducing cell cycle arrest, Cancer Lett. 310 (2) (2011) 160–169.
[10] T.C. Chang, D. Yu, Y.S Lee, E.A. Wentzel, D.E Arking, K.M West, C.V. Dang, A. Thomas-Tikhonenko, J.T Mendell, Widespread microRNA repression by Myc contributes to tumorigenesis, Nat. Genet. 40 (1) (2008) 43–50.
[11] B. Wang, S.H. Hsu, X. Wang, H. Kutay, H.K Bid, J. Yu, R.K Ganju, S.T Jacob, M. Yuneva, K. Ghoshal, Reciprocal regulation of microRNA-122 and c-Myc in hepatocellular cancer: role of E2F1 and transcription factor dimerization partner 2, Hepatology 59 (2) (2014) 555–566.
[12] H. Wang, P. Agarwal, S. Zhao, J. Yu, X. Lu, X. He, A Near-infrared laser-activated "nanobomb" for breaking the barriers to MicroRNA delivery, Adv. Mater. 28 (9) (2016) 1723 (Weinheim).
[13] C. Chen, S. Zhao, A. Karnad, J.W Freeman, The biology and role of CD44 in cancer progression: therapeutic implications, J. Hematol. Oncol. 11 (1) (2018) 64.
[14] J.C Wischhusen, S.M Chowdhury, T. Lee, H. Wang, S. Bachawal, R. Devulapally, R. Afjei, U.K Sukumar, R. Paulmurugan, Ultrasound-mediated delivery of miRNA-122 and anti-miRNA-21 therapeutically immunomodulates murine hepatocellular carcinoma *in vivo*, J. Control. Release 321 (2020) 272–284 official journal of the Controlled Release Society.
[15] C. Coulouarn, V.M. Factor, J.B Andersen, M.E Durkin, S.S. Thorgeirsson, Loss of miR-122 expression in liver cancer correlates with suppression of the hepatic phenotype and gain of metastatic properties, Oncogene 28 (40) (2009) 3526–3536.
[16] G. Xu, Y. Zhang, J. Wei, W. Jia, Z. Ge, Z. Zhang, X. Liu, MicroRNA-21 promotes hepatocellular carcinoma HepG2 cell proliferation through repression of mitogen-activated protein kinase-kinase 3, BMC Cancer 13 (1) (2013) 469.
[17] F. Meng, R. Henson, H. Wehbe–Janek, K. Ghoshal, S.T Jacob, T. Patel, MicroRNA-21 regulates expression of the PTEN tumor suppressor gene in human hepatocellular cancer, Gastroenterology 133 (2) (2007) 647–658..
[18] Y. Liu, J.T Bailey, M. Abu-Laban, S. Li, C. Chen, A.B Glick, D.J. Hayes, Photocontrolled miR-148b nanoparticles cause apoptosis, inflammation and regression of Ras induced epidermal squamous cell carcinomas in mice, Biomaterials 256 (120212) (2020) 120212.
[19] Y. Xu, A. Karmakar, W.E. Heberlein, T. Mustafa, A.R Biris, A.S Biris, Multifunctional magnetic nanoparticles for synergistic enhancement of cancer treatment by combinatorial radio frequency thermolysis and drug delivery, Adv. Healthc. Mater. 1 (4) (2012) 493–501.
[20] L. Wang, P. Zhang, J. Shi, Y. Hao, D. Meng, Y. Zhao, Y. Yanyan, D. Li, J. Chang, Z. Zhang, Radiofrequency-triggered tumor-targeting delivery system for theranostics application, ACS Appl. Mater. Interfaces 7 (10) (2015) 5736–5747.
[21] P.T Yin, B.P. Shah, K.B. Lee, Combined magnetic nanoparticle-based MicroRNA and hyperthermia therapy to enhance apoptosis in brain cancer cells, Small 10 (20) (2014) 4106–4112 n/a-n/a.
[22] J.H Lee, J.T Jang, J.S Choi, S.H Moon, S.H Noh, J.W Kim, J.G Kim, I.S. Kim, K.I. Park, J. Cheon, Exchange-coupled magnetic nanoparticles for efficient heat induction, Nat. Nanotechnol. 6 (7) (2011) 418–422.
[23] M. Abu-Laban, R.R. Kumal, J. Casey, J. Becca, D. Lamaster, C.N. Pacheco, D.G. Sykes, L. Jensen, L.H. Haber, Comparison of thermally actuated retro-diels-alder release groups for nanoparticle based nucleic acid delivery, J. Colloid Interface Sci. 526 (2018) 312–321.
[24] R. Rupaimoole, F.J. Slack, MicroRNA therapeutics: towards a new era for the management of cancer and other diseases, Nat. Rev. Drug Discov. 16 (3) (2017) 203–222.
[25] E. Aprà, E.J. Bylaska, W.A. De Jong, N. Govind, K. Kowalski, T.P. Straatsma, M. Valiev, H.J.J. Van Dam, Y. Alexeev, J. Anchell, V. Anisimov, F.W. Aquino, R. Atta-Fynn, J. Autschbach, N.P. Bauman, J.C. Becca, D.E. Bernholdt, K. Bhaskaran-Nair, S. Bogatko, P. Borowski, J. Boschen, J. Brabec, A. Bruner, E. Cauët, Y. Chen, G.N. Chuev, C.J. Cramer, J. Daily, M.J.O. Deegan, T.H. Dunning, M. Dupuis, K.G. Dyall, G.I. Fann, S.A. Fischer, A. Fonari, H. Früchtl, L. Gagliardi, J. Garza, N. Gawande, S. Ghosh, K. Glaesemann, A.W. Götz, J. Hammond, V. Helms, E.D. Hermes, K. Hirao, S. Hirata, M. Jacquelin, L. Jensen, B.G. Johnson, H. Jónsson, R.A. Kendall, M. Klemm, R. Kobayashi, V. Konkov, S. Krishnamoorthy, M. Krishnan, Z. Lin, R.D. Lins, R.J. Littlefield, A.J. Logsdail, K. Lopata, W. Ma, A.V. Marenich, J. Martin Del Campo, D. Mejia-Rodriguez, J.E. Moore, J.M. Mullin, T. Nakajima, D.R. Nascimento, J.A. Nichols, P.J. Nichols, J. Nieplocha, A. Otero-De-La-Roza, B. Palmer, A. Panyala, T. Pirojsirikul, B. Peng, R. Peverati, J. Pittner, L. Pollack, R.M. Richard, P. Sadayappan, G.C. Schatz, W.A. Shelton, D.W. Silverstein, D.M.A. Smith, T.A. Soares, D. Song, M. Swart, H.L. Taylor, G.S. Thomas, V. Tipparaju, D.G. Truhlar, K. Tsemekhman, T. Van Voorhis, Á. Vázquez-Mayagoitia, P. Verma, O. Villa, A. Vishnu, K.D. Vogiatzis, D. Wang, J.H. Weare, M.J. Williamson, T.L. Windus, K. Woliński, A.T. Wong, Q. Wu, C. Yang, Q. Yu, M. Zacharias, Z. Zhang, Y. Zhao, R.J. Harrison, NWChem: past, present, and future, J. Chem. Phys. 152 (18) (2020) 184102.
[26] A.D. Becke, Density-functional thermochemistry. III. The role of exact exchange, J. Chem. Phys. 98 (7) (1993) 5648–5652.
[27] S.H. Vosko, L. Wilk, M. Nusair, Accurate spin-dependent electron liquid correlation energies for local spin density calculations: a critical analysis, Can. J. Phys. 58 (8) (1980) 1200–1211.
[28] C. Lee, W. Yang, R.G. Parr, Development of the Colle-Salvetti correlation-energy formula into a functional of the electron density, Phys. Rev. B 37 (2) (1988) 785–789.
[29] P.J. Stephens, F.J. Devlin, C.F. Chabalowski, M.J. Frisch, Ab initio calculation of vibrational absorption and circular dichroism spectra using density functional force fields, J. Phys. Chem. 98 (45) (1994) 11623–11627.
[30] M. Abu-Laban, P. Hamal, J.H. Arrizabalaga, A. Forghani, A.S. Dikkumbura, R.R. Kumal, L.H. Haber, D.J. Hayes, Combinatorial delivery of miRNA-nanoparticle conjugates in human adipose stem cells for amplified osteogenesis, Small 15 (50) (2019) 1902864.
[31] J.S. Casey, J.H. Arrizabalaga, M. Abu-Laban, J.C. Becca, B.J. Rose, K.T. Strickland, J.B. Bursavich, J.S. McCann, C.N. Pacheco, L. Jensen, A. Attaluri, D.J. Hayes, Alternating magnetic field mediated release of fluorophores from magnetic nanoparticles by hysteretic heating, J. Colloid Interface Sci. 571 (2020) 348–355.

[32] T.T.T. N'Guyen, H.T.T. Duong, J. Basuki, V. Montembault, S. Pascual, C. Guibert, J. Fresnais, C. Boyer, M.R. Whittaker, T.P. Davis, L. Fontaine, Functional iron oxide magnetic nanoparticles with hyperthermia-induced drug release ability by using a combination of orthogonal click reactions, Angew. Chem. Int. Ed. 52 (52) (2013) 14152–14156.

[33] R. Massart, Preparation of aqueous magnetic liquids in alkaline and acidic media, IEEE Trans. Magn. 17 (2) (1981) 1247–1248.

[34] J.H. Arrizabalaga, J.S. Casey, J.C. Becca, L. Jensen, D.J. Hayes, Comparison of thermoresponsive Diels-Alder linkers for the release of payloads from magnetic nanoparticles via hysteretic heating, JCIS Open 4 (2021) 100034.

[35] H. Cao, J. He, L. Deng, X. Gao, Fabrication of cyclodextrin-functionalized superparamagnetic Fe_3O_4/amino-silane core–shell nanoparticles via layer-by-layer method, Appl. Surf. Sci. 255 (18) (2009) 7974–7980.

[36] R.E. Rosensweig, Heating magnetic fluid with alternating magnetic field, J. Magn. Magn. Mater. 252 (1-3) (2002) 370–374.

[37] F. Soetaert, S.K. Kandala, A. Bakuzis, R. Ivkov, Experimental estimation and analysis of variance of the measured loss power of magnetic nanoparticles, Sci. Rep. 7 (1) (2017) 6661.

[38] J.H. Arrizabalaga, M.U. Nollert, Riboflavin-UVA crosslinking of amniotic membranes and its influence on the culture of adipose-derived stem cells, J. Mech. Behav. Biomed. Mater. 106 (2020) 103729.

[39] J.P. Fortin, C. Wilhelm, J. Servais, C. Ménager, J.-C. Bacri, F. Gazeau, Size-sorted anionic iron oxide nanomagnets as colloidal mediators for magnetic hyperthermia, J. Am. Chem. Soc. 129 (9) (2007) 2628–2635.

[40] Q. Li, C.W. Kartikowati, S. Horie, T. Ogi, T. Iwaki, K. Okuyama, Correlation between particle size/domain structure and magnetic properties of highly crystalline Fe_3O_4 nanoparticles, Sci. Rep. 7 (1) (2017) 9894.

[41] R. Chen, M.G. Christiansen, P. Anikeeva, Maximizing hysteretic losses in magnetic ferrite nanoparticles via model-driven synthesis and materials optimization, ACS Nano 7 (10) (2013) 8990–9000.

[42] V. Guner, K.S. Khuong, A.G. Leach, P.S. Lee, M.D. Bartberger, K.N. Houk, A standard set of pericyclic reactions of hydrocarbons for the benchmarking of computational methods: the performance of ab initio, density functional, CASSCF, CASPT2, and CBS-QB3 methods for the prediction of activation barriers, reaction energetics, and transition state geometries, J. Phys. Chem. A 107 (51) (2003) 11445–11459.

[43] R.C. Boutelle, B.H. Northrop, Substituent effects on the reversibility of furan–maleimide cycloadditions, J. Org. Chem. 76 (19) (2011) 7994–8002.

[44] W.L. Delano, PyMOL: an open-source molecular graphics tool, CCP4 Newslett. Protein Crystallogr. 40 (1) (2002) 82–92.

[45] R.R. Kumal, M. Abu-Laban, P. Hamal, B. Kruger, H.T. Smith, D.J. Hayes, L.H. Haber, Near-infrared photothermal release of siRNA from the surface of colloidal gold–silver–gold core–shell–shell nanoparticles studied with second-harmonic generation, J. Phys. Chem. C 122 (34) (2018) 19699–19704.

[46] A. Kumar, A. Attaluri, R. Mallipudi, C. Cornejo, D. Bordelon, M. Armour, K. Morua, T.L. Deweese, R. Ivkov, Method to reduce non-specific tissue heating of small animals in solenoid coils, Int. J. Hyperth. 29 (2) (2013) 106–120.

[47] G.M. Goncher, C.A. Parsons, C.B. Harris, Photochemistry on rough metal surfaces, J. Phys. Chem. 88 (19) (1984) 4200–4209.

[48] Z. Jiang, J. Zhang, F. Chen, Y. Sun, MiR-148b suppressed non-small cell lung cancer progression via inhibiting ALCAM through the NF-κB signaling pathway, Thorac. Cancer 11 (2) (2020) 415–425.

[49] N. Rath, M.F. Olson, Rho-associated kinases in tumorigenesis: re-considering ROCK inhibition for cancer therapy, EMBO Rep. 13 (10) (2012) 900–908.

[50] H. Luo, C. Liang, MicroRNA-148b inhibits proliferation and the epithelial-mesenchymal transition and increases radiosensitivity in non-small cell lung carcinomas by regulating ROCK1, Exp. Ther. Med. 15 (4) (2018) 3609–3616.

[51] D. Cimino, C. De Pittà, F. Orso, M. Zampini, S. Casara, E. Penna, E. Quaglino, M. Forni, C. Damasco, E. Pinatel, R. Ponzone, C. Romualdi, C. Brisken, M. De Bortoli, N. Biglia, P. Provero, G. Lanfranchi, D. Taverna, miR148b is a major coordinator of breast cancer progression in a relapse-associated microRNA signature by targeting ITGA5, ROCK1, PIK3CA, NRAS, and CSF1, FASEB J. 27 (3) (2013) 1223–1235.

[52] F. Orso, L. Quirico, F. Virga, E. Penna, D. Dettori, D. Cimino, R. Coppo, E. Grassi, A.R. Elia, D. Brusa, S. Deaglio, M.F. Brizzi, M.B. Stadler, P. Provero, M. Caselle, D. Taverna, miR-214 and miR-148b targeting inhibits dissemination of melanoma and breast cancer, Cancer Res. 76 (17) (2016) 5151–5162.